Assessing the impact of ambient fabrication temperature on the performance of planar CH3NH3PbI3 perovskite solar cells

Zuzanna Molenda, Sylvain Chambon, Dario Bassani, Lionel Hirsch

FULL PAPER

Assessing the impact of ambient fabrication temperature on the performance of planar $CH_3NH_3PbI_3$ perovskite solar cells

Zuzanna Molenda[a,c], Sylvain Chambon[b], Dario M. Bassani* [c], Lionel Hirsch*[a]

[a] MSc Z. Molenda, Dr. L. Hirsch
Univ. de Bordeaux, CNRS, Bordeaux INP
IMS, UMR 5218, ENSCBP, F-33405 Talence, France
E-mail: lionel.hirsch@ims-bordeaux.fr
[b] Dr. S. Chambon
LIMMS/CNRS-IIS (IRL2820)
Institute of Industrial Science
The University of Tokyo
4-6-1 Komaba, Meguro-ku, Tokyo, 153-8505, Japan
[c] Dr. D. M. Bassani
Univ. de Bordeaux, CNRS, Bordeaux INP
ISM, UMR 5255, F-33405 Talence, France
E-mail: dario.bassani@u-bordeaux.fr

Abstract: The ambient fabrication temperature inside the glove box is found to play an important role in determining the overall power conversion efficiency in solar cells based on $CH_3NH_3PbI_3$ (MAPI) hybrid organic-inorganic perovskites. We find that a variation of the ambient temperature of only 10°C during the fabrication process has a crucial impact on both the reproducibility and the efficiency of the devices. Atomic Force Microscopy, XRD, UV-Vis absorption and electroluminescence have been carried out to investigate the origin of this behavior. We conclude that the partial vapor pressure variation of the solvent impacts the crystallization process inducing an increase density of traps within the bandgap of the perovskite.

Introduction

In recent years, hybrid organic-inorganic perovskites (HOIP) have become widely used as materials for photovoltaic application due to their excellent optoelectronic properties[1–5] and uncomplicated device preparation[6,7]. Within 12 years of research on HOIP-based solar cells, laboratory device efficiencies increased from 3.8% to 22.8% for single junction solar cells[8,9] and reached 25.2% for tandem perovskite-silicon solar cells[10]. The tremendous improvement in such a short time is in part due to past work in the field of organic photovoltaics and dye sensitized solar cells with which many operational and preparative aspects are similar for those devices. To date, the most common method of perovskite solar cells fabrication on the laboratory scale is spin coating.[11–13] Other approaches include dip-coating[14], drop casting[15], doctor blade[16,17] and evaporation[18].

Improving the performance and understanding of perovskite based solar cells requires that results be reproducible. To this end, procedure protocols in the perovskite solar cells field started appearing a few years ago.[19] Nevertheless, precise experimental condition parameters are sometimes neglected as they are not identified as being of importance. One of these is the ambient temperature at which the solution containing the perovskite precursors is spin coated. This temperature is most commonly that found inside the glove box and can vary throughout the day and across seasons by around 10°C. In 2020, the group of Han et al.[20] demonstrated that the performance of perovskite based light emitting diodes (LEDs) depended on the ambient temperature over a range of 21-31°C. These authors observed different crystallographic orientation of the Ruddlesden-Popper phase perovskites with the formula of $PEA_2MA_{n-1}Pb_nBr_{3n-1}$ whose formation depends on the temperature in the glovebox during the solution processing. Temperature around 21°C favor crystal orientations parallel to the substrate, whereas higher temperatures favor cubic crystals that grow vertical with respect to the substrate. These compositional and structural changes influence the electrical and optical properties, which result in different device performance. Moreover, the standard deviation in observed devices efficiencies increases from 9.9% to 71.4% with increasing temperature.

In the case of HOIPs solar cell devices, basic studies including solvent engineering[21–23], compositional engineering[24,25] and architecture design of the PSCs[18,26,27] have been conducted on methylammonium lead triiodide ($CH_3CN_3PbI_3$) materials due to their relatively simple structure and good efficiency for non-doped, single cation and single-halide perovskite solar cells. Herein, we show that the ambient temperature during perovskite solar cell preparation is a crucial parameter that has a profound effect on the efficiency and standard deviation. Our findings suggest that variations in the crystal quality are responsible for the solar cells' decreased performance when prepared at higher ambient temperatures. In particular, increased defect density of the perovskite layer fabricated at 30°C reduces the average efficiency by the factor of over 2.5.

Results and Discussion

To study the impact of ambient temperature on the photovoltaic performances, a total of 85 perovskite solar cell devices were prepared in 3 batches at 3 different temperatures inside the glovebox: 20°C, 25°C and 30°C. These temperatures can typically occur in a laboratory over different seasons or even during one day. In the glove box, where these samples were prepared, the typical ambient temperature can vary from 21 to 25°C throughout the experiment time. In the study presented herein, the PSCs of devices with an inverted architecture using MAPI as an active layer sandwiched between poly(triaryl amine) (PTAA) as a hole transporting layer (HTL) and phenyl-C_{61}-butyric acid methyl ester (PCBM) as an electron transporting layer (ETL)

were investigated (Figure 1). In order to perform statistical analysis, for each temperature, at least 15 solar cell samples were taken into account, prepared in 2 batches.

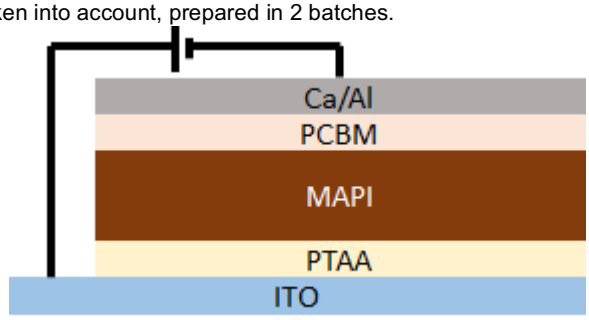

Figure 1. Schematic representation of the device architecture.

The power conversion efficiency (*PCE*), open circuit voltage (V_{oc}) and short circuit current (J_{sc}) of solar cell devices prepared at different ambient temperatures inside of the glovebox are shown in Figure 2. One can notice that the *PCE* is the highest for the devices prepared at 20°C and 25°C (on average 11.0 ± 1.7 % and 9.2 ± 2.2 % respectively). In contrast, cells prepared at a temperature of 30°C consistently show efficiencies reaching only 4.3 ± 2.1 % on average. Moreover, it is worth noting that the standard deviation is the lowest for the samples prepared at 20°C and largest at 30°C. Similarly, J_{sc} shows the highest average value and the lowest standard deviation for the fabrication at 20°C (14.8 ± 0.5 mA cm^{-2}), whereas devices processed at 25°C and 30°C present lower J_{sc} and higher standard deviation, 14.0 ± 1.4 mA cm^{-2} 10.4 ± 3.0 mA cm^{-2}, respectively. The V_{oc} has a comparable value for both 20°C and 25°C (0.99 ± 0.02 V and 0.99 ± 0.01 V, respectively), and a significant decrease is observed at 30°C (0.79 ± 0.17 V).

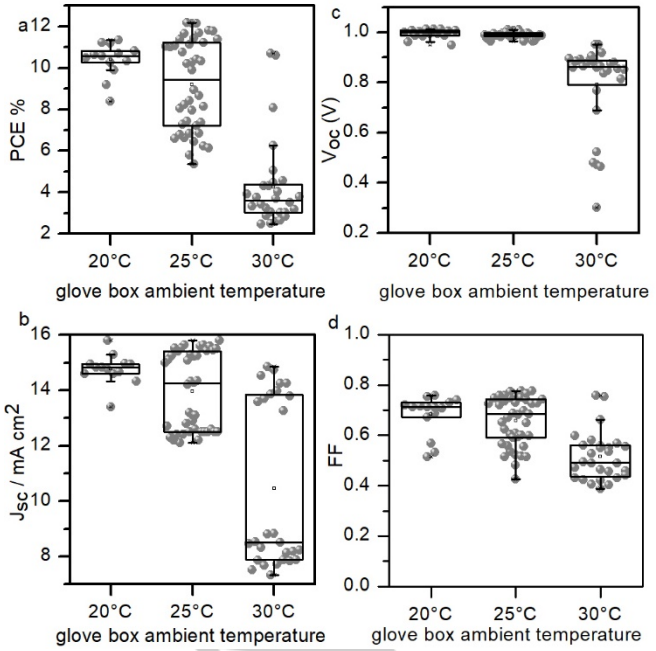

Figure 2. Power conversion efficiency (a), open circuit voltage (b), short circuit current (c) and fill factor (d) of 85 perovskite solar cells prepared in 3 batches at different ambient temperatures.

The electrical characterization of devices prepared at different temperatures suggests that higher quality perovskite crystals may be formed at lower ambient temperatures and that this can contribute to increased *PCE* through more efficient charge extraction. Processing the active layer at lower ambient temperature would be expected to lower the concentration of defects. As a consequence, the number of recombination centers decreases, thus minimizing shunt losses induced by this recombination. This mechanism impacts directly all the other solar cells parameters, such as V_{oc} and J_{sc}. Additionally, one must note that when the temperature is not controlled, i.e. considering all the devices prepared for this experiment, the standard deviation of the PCE reaches 42%.

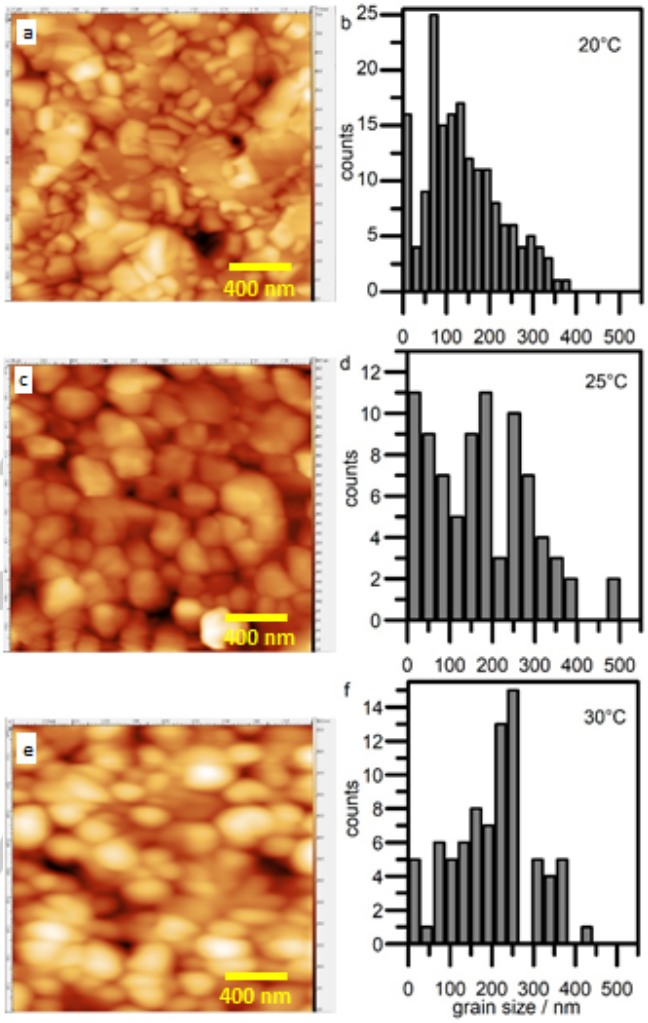

Figure 3. Atomic Force Microscopy images of the 190 nm thick perovskite layer spin coated onto a glass/PTAA substrate, deposited at 20°C (a), 25°C (c) and 30°C (e) and corresponding distributions of the grain size, defined as the distance between the two most distanced points on the AFM images for samples prepared at 20°C (b), 25°C (d) and 30°C (f).

In search of the reason for the difference in the electronic properties for devices prepared at different temperatures, the morphology of the active layers was probed using atomic force microscopy. AFM images for different samples are presented in Figure 3. In general, we find that the crystalline grain shape is more clearly visible for the lowest temperature probed (Figure 3a), while for samples prepared at 25°C and 30°C (Figure 3b, c) the grains edges are less sharp and more rounded. Indeed, the root means square (*RMS*) roughness is the lowest for the highest fabrication temperature (1.0 nm), slightly higher for 25°C (1.3 nm) and the highest for 20°C (2.2 nm). Even though the grain size distribution (Figure 3. d-f) indicates that the smallest grain sizes are obtained at 20°C (~100 nm), these grains appear to be better

defined than the larger grains obtained at higher temperatures (~150 nm for 25°C and ~250 nm for 30°C).

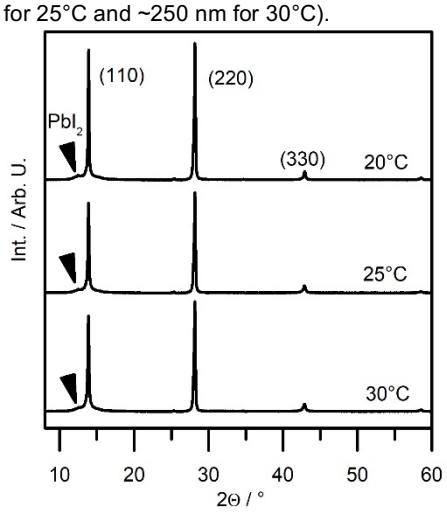

Figure 4. X-ray diffraction pattern of the 190 nm thick perovskite layer spin coated onto a PTAA layer deposited on a glass slide at different ambient temperatures.

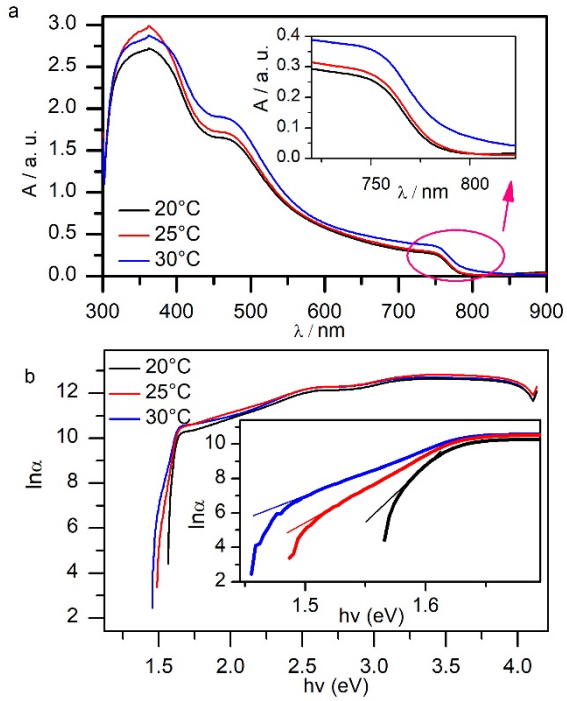

Figure 5. Absorption spectra in the visible light of the 190 nm thick perovskite layer spin coated onto a PTAA layer deposited on a glass slide at different ambient temperatures. The curves are the average of 3 samples per each ambient temperature

The X-ray diffraction pattern (XRD) for active layer prepared at the three different ambient temperatures exhibit four peaks typical for MAPI at 14.1°, 28.4°, 43.2° and 58.9° (Figure 4). These correspond respectively to the (110), (220), (330) and (440) crystallographic planes of the tetragonal structure[28]. A small peak at 12.7° reveals the presence of trace amounts of PbI_2 present in the perovskite structure of all three samples. The main difference between the patterns is the peaks' intensity, especially visible for the peaks at 14.1° and 28.4°. We observed that the intensity is the highest for the samples prepared at 20°C, which suggests that this improves crystallinity. Using the Scherrer equation, we can quantify the differences in the crystal quality[29,30]. The crystal domain size, calculated from the full width at half maximum (FWHM), was the highest for the samples fabricated at 20°C (average = 54.3 nm), and lower for those sample fabricated at 25°C and 30°C (36.0 nm and 35.1 nm, respectively).

The absorption spectra of samples fabricated at 3 different temperatures on a PTAA-coated glass substrate are shown in Figure 5. The spectra are typical for MAPI[31,32], with an absorption threshold at 752 nm corresponding to a bandgap of 1.65 eV that is comparable to literature reports[33–35]. However, one can notice that small differences are present in the absorption edge (Figure 5a, inset) and that the spectrum corresponding to the 30°C sample exhibits a significant Urbach's tail.

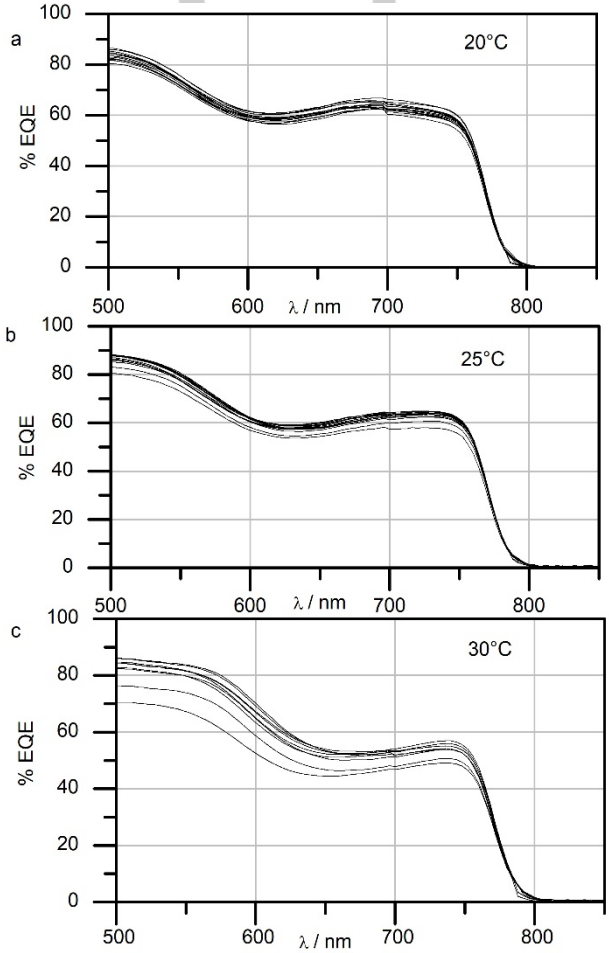

Figure 6. External quantum efficiency spectra for MAPI solar cells fabricated at different temperatures.

Typically, Urbach's tail is associated to the presence of impurities, disorder, or defects in a thin film of a semiconductor[36]. The quantitative representation of these properties is the Urbach energy (E_U). It was showed that high E_U values correspond to higher charge recombination rates, which contribute to the decrease of the perovskite solar cell's efficiency[37].

E_U was extracted by plotting the natural logarithm of the absorption coefficient α, according to:

$$\alpha = \alpha_0 exp\left(h\nu {E_U}^{-1}\right) \quad (1)$$

$$ln\alpha = \ln(\alpha_0) + \left(h\nu {E_U}^{-1}\right) \quad (2)$$

where h is Planck's constant, ν is the frequency of light and α_0 is a constant. The values of E_U extracted from the plots presented in the Figure 5b are 26 meV, 28 meV and 83 meV, respectively,

for the samples prepared at 20°C, 25°C and 30°C. The lowest E_U reported for MAPI by De Wolf et al.[38] was 15 meV, while Moyes and Roy[39] reached values of 25 and 41 meV. Therefore, it can be concluded that the E_U values obtained here for samples prepared at 20°C and 25°C are relatively low and comparable to those reported elsewhere. In contrast, the significantly larger E_U for the sample prepared at 30°C suggests the presence of much larger charge recombination rates, presumably linked to the increased defect densities and/or a more highly disordered crystal structure.

The EQE spectra of all the samples investigated (Figure 6) present a broad contribution of the visible photons to the photocurrent that is consistent with the absorption spectra in Figure 5. The J_{sc} calculated from the EQE measurement are in agreement with those obtained from the *J-V* curves (see below). A significant efficiency difference can be noticed for wavelengths at ca. 700 nm. It reaches the highest value at 20°C (63 ± 1.6%) and only slightly lower for 25°C (62 ± 1.7%). A more significant drop in efficiency is observed for samples prepared at 30°C, where the EQE value is around 51 ± 2.4%. Inefficient photon to electron conversion of red light can be linked to non-radiative losses, in agreement with the very low electroluminescence observed from samples produced at 30°C.

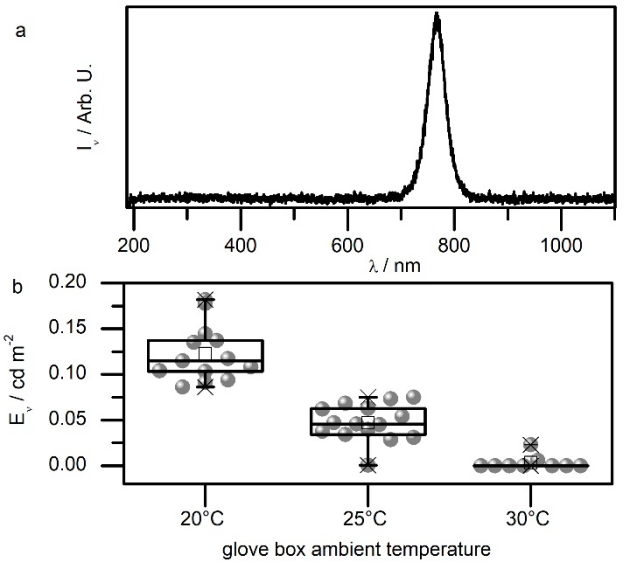

Figure 7. a) EL spectrum from the sample emmiting the highest intesity light; b) electroluminescence at +2.5 V of the devices produced in different ambient temperatures.

The electroluminescence of MAPI devices typically provides information on the non-radiative recombination processes responsible for the shunt losses[40,41]. These losses can occur as a result of Auger recombination, band-tail recombination, electron-phonon coupling and defect-assisted recombination[42]. They impact the open circuit voltage (V_{oc}), short circuit current (J_{sc}) and fill factor (*FF*), which results in a decrease of the overall solar cell performance. Efficient non-radiative recombination may additionally lead to a significant deterioration of the solar cell's stability, which is an important factor for their industrialization[43,44]. The electroluminescence of the solar cells prepared at different ambient temperatures was measured and is reported in Figure 7. Radiative emission was observed between the red and near infrared range with a λ_{max} at ca. 770 nm (Figure 7a). The highest luminosity E_V was observed for the samples prepared at 20°C (0.12 ± 0.03 cd m^{-2}) and over two-fold lower for those samples prepared at 25°C (0.05 ± 0.02 cd m^{-2}). Samples prepared at 30°C exhibited negligible emission (Figure 7b). The decrease of the luminosity indicates the presence of significant losses associated with non-radiative charge recombination processes. Combining results from electroluminescence experiments with the observations from AFM, XRD and analysis of the absorption spectra suggests that samples prepared at higher ambient temperatures show more efficient charge recombination taking place at defect sites within the crystal structure and/or on the grain boundaries. In agreement with this, the V_{oc} distribution presented in Figure 2b shows a significant decrease for solar cells prepared at 30°C. The decrease in V_{oc} can be rationalized by the splitting the quasi-Fermi levels of the electrons and holes during illumination. The difference between these levels defines the maximum theoretical V_{oc} [45,46] and non-radiative losses effectively limit the split of the quasi-Fermi levels, thus reducing the achievable V_{oc}.

Conclusion

This work highlights the impact of the ambient temperature on the performance of planar solar cells prepared with MAPI as an active layer. The observed decrease in *PCE* is related to changes in morphology as evidenced from the comparison of the AFM images, XRD and presence of Urbach's tail for perovskite layers processed at 30°C. These results therefore confirm the importance of the ambient temperature on the density of structural defects in MAPI. This temperature range obviously depends on the solvent used and on the composition of the active layer. Electroluminescence analysis suggests that these defects act as non-radiative recombination centers that are likely to be the cause of the decrease in V_{oc}, J_{sc}, *FF* and, consequently, the overall performance of the solar cells. Amongst all the devices investigated, those prepared at 20°C exhibit the best photo conversion efficiency. The performance drops dramatically when the temperature is incremented even by only 10°C. Such a small increase in ambient temperature can easily occur in glove boxes located in most laboratory environments due to seasonal or daily fluctuations as a result of thermal treatments (eg annealing). This should come as no surprise since the crystallization process, which is an important factor in determining the overall performance, is related to the crystallization temperature and also to the partial vapor pressure of the solvent used. The latter typically increases with increasing temperature[47], thereby affecting the evaporation rate during the spin coating process.

Experimental Section

Materials. Lead (II) acetate trihydrate ($PbAc_2 \cdot 3H_2O$, 5N) was purchased from Sigma Aldrich. Methylammonium iodide (CH_3CN_3I, >4N) was purchased from GreatCell Solar Materials. Poly(triaryl amine) (PTAA) with molecular weight of 17 kDa was purchased from Solaris Chem. Phenyl-C_{61}-butyric acid methyl ester (PCBM, 4N) was purchased from Solaris. Anhydrous toluene, anhydrous N,N-Dimethylformamide (DMF) and anhydrous chlorobenzene (CB) were purchased from Sigma Aldrich.

Device fabrication. Glass substrates covered with a thin layer of ITO (10 Ω/sq) were cleaned in the sonication bath first with the Hellmanex™ III (Sigma Aldrich) and in the DI water for 15 minutes each, then in isopropanol (4N) for 10 min. Subsequently they were treated with UV-ozone for 15 minutes. 4.5 mg PTAA was dissolved in toluene, stirred at RT

overnight and filtered with 0.45µm PTFE filter. The 15 nm thick PTAA layer was spin coated onto clean substrates at spin rate 6000 rpm for 30 s and dried for 10 min at 100°C. Perovskite precursor solution was prepared by dissolving 0.72 M $PbAc_2 \cdot 3H_2O$ and 2.2 M MAI in DMF and stirred at room temperature for 30 min. The solution was filtered with 0.45µm PTFE filter and spin coated at spin rate 6000 rpm for 2 min. The sample was then dried at RT for 3 min and annealed for 25 min at 100°C. The perovskite film thickness was around 190 nm. 20 mg PCBM was dissolved in CB and stirred overnight at 50°C. After being filtered with 0.45µm PTFE filter, the solution was spin coated at spin rate 2500 nm for 1 min, resulting in layer thickness of around 90 nm. The electrodes 30 nm Ca and 70 nm Al were thermally evaporated, using a mask that defined the area of the cells (10.5 mm^2).

Characterization IV curves were registered using Keithley 2400 source meter unit (SMU) controlled by a LabView program. The solar cell devices were scanned from -1 V to 1.2 V with the rate of 10 mV/s. the HMI lamp was used with the AM 1.5G spectrum and light intensity 100 mW/cm2. The emission energy was found using Ocean Optics High Resolution Spectrometer HR2000, while the luminescence was measured using Keithley multimeter connected to the photosensor amplifier Hamamtsu C9329. The calibration of the photodetector signal to luminescence was performed using a luminance meter Konica Minolta LS-100. The external quantum efficiency (EQE) was measured using Bentham PVE300 Photovoltaic Characterization setup, equipped with a dual xenon/halogen light sources optically chopped illuminator system. For the AFM images, Bruker NanoScope was used. X-ray diffraction (XRD) was realized using Bruker D2 Phaser and the absorption spectra using Shimadzu UV-3600 Plus UV-Vis-NIR Spectrophotometer.

Acknowledgements

Financial support from the ANR with the HYPERSOL project under grant ANR-18-CE05-0021-01 is gratefully acknowledged. The Aquitaine government is thanked for support through grant 2019-1R1M08.

Keywords: Perovskite solar cells • Ambient temperature • Methylammonium lead iodide • Defects • Non-radiative losses

[1] M. A. Green, Y. Jiang, A. M. Soufiani, A. Ho-Baillie, *J. Phys. Chem. Lett.* **2015**, *6*, 4774.

[2] M. B. Johnston, L. M. Herz, *Acc. Chem. Res.* **2016**, *49*, 146.

[3] A. Miyata, A. Mitioglu, P. Plochocka, O. Portugall, J. T. W. Wang, S. D. Stranks, H. J. Snaith, R. J. Nicholas, *Nat. Phys.* **2015**, *11*, 582.

[4] D. Shi, V. Adinolfi, R. Comin, M. Yuan, E. Alarousu, A. Buin, Y. Chen, S. Hoogland, A. Rothenberger, K. Katsiev, Y. Losovyj, X. Zhang, P. A. Dowben, O. F. Mohammed, E. H. Sargent, O. M. Bakr, *Science* **2015**, *347*, 519.

[5] M. J. P. Alcocer, T. Leijtens, L. M. Herz, A. Petrozza, H. J. Snaith, *Science* **2013**, *342*, 341.

[6] F. Fu, T. Feurer, T. Jäger, E. Avancini, B. Bissig, S. Yoon, S. Buecheler, A. N. Tiwari, *Nat. Commun.* **2015**, *6*, 1.

[7] A. Mei, X. Li, L. Liu, Z. Ku, T. Liu, Y. Rong, M. Xu, M. Hu, J. Chen, Y. Yang, M. Grätzel, H. Han, *Science* **2014**, *345*, 295.

[8] M. T, K. A, T. K, S. Y, *J. Am. Chem. Soc.* **2009**, *131*, 6050.

[9] A. Y. Alsalloum, B. Turedi, K. Almasabi, X. Zheng, R. Naphade, S. D. Stranks, O. F. Mohammed, O. M. Bakr, *Energy Environ. Sci.* **2021**, DOI 10.1039/d0ee03839c.

[10] F. Sahli, J. Werner, B. A. Kamino, M. Bräuninger, R. Monnard, B. Paviet-Salomon, L. Barraud, L. Ding, J. J. Diaz Leon, D. Sacchetto, G. Cattaneo, M. Despeisse, M. Boccard, S. Nicolay, Q. Jeangros, B. Niesen, C. Ballif, *Nat. Mater.* **2018**, *17*, 820.

[11] P. Zhao, B. J. Kim, X. Ren, D. G. Lee, G. J. Bang, J. B. Jeon, W. Bin Kim, H. S. Jung, *Adv. Mater.* **2018**, *30*, 1.

[12] C. G. Wu, C. H. Chiang, Z. L. Tseng, M. K. Nazeeruddin, A. Hagfeldt, M. Grätzel, *Energy Environ. Sci.* **2015**, *8*, 2725.

[13] R. Naphade, B. Zhao, J. M. Richter, E. Booker, S. Krishnamurthy, R. H. Friend, A. Sadhanala, S. Ogale, *Adv. Mater. Interfaces* **2017**, *4*, 1.

[14] J. Burschka, N. Pellet, S. J. Moon, R. Humphry-Baker, P. Gao, M. K. Nazeeruddin, M. Grätzel, *Nature* **2013**, *499*, 316.

[15] J. H. Im, I. H. Jang, N. Pellet, M. Grätzel, N. G. Park, *Nat. Nanotechnol.* **2014**, *9*, 927.

[16] Y. Deng, Q. Wang, Y. Yuan, J. Huang, *Mater. Horizons* **2015**, *2*, 578.

[17] H. Ying, Y. Liu, Y. Dou, J. Zhang, Z. Wu, Q. Zhang, Y. B. Cheng, J. Zhong, *Front. Optoelectron.* **2020**, *13*, 272.

[18] M. Liu, M. B. Johnston, H. J. Snaith, *Nature* **2013**, *501*, 395.

[19] M. Saliba, J. P. Correa-Baena, C. M. Wolff, M. Stolterfoht, N. Phung, S. Albrecht, D. Neher, A. Abate, *Chem. Mater.* **2018**, *30*, 4193.

[20] Y. Han, J. Wang, C. G. Bischak, S. Kim, K. Lee, D. Shin, M. J. Lee, D. S. Ginger, I. Hwang, *ACS Photonics* **2020**, *7*, 2489.

[21] N. Ahn, D. Y. Son, I. H. Jang, S. M. Kang, M. Choi, N. G. Park, *J. Am. Chem. Soc.* **2015**, *137*, 8696.

[22] H. N. Chen, Z. H. Wei, H. X. He, X. L. Zheng, K. S. Wong, S. H. Yang, *Adv. Energy Mater.* **2016**, *6*, DOI 10.1002/aenm.201502087.

[23] N. J. Jeon, J. H. Noh, Y. C. Kim, W. S. Yang, S. Ryu, S. Il Seok, *Nat. Mater.* **2014**, *13*, 897.

[24] Z. Yang, C. C. Chueh, P. W. Liang, M. Crump, F. Lin, Z. Zhu, A. K. Y. Jen, *Nano Energy* **2016**, *22*, 328.

[25] N. J. Jeon, J. H. Noh, W. S. Yang, Y. C. Kim, S. Ryu, J. Seo, S. Il Seok, *Nature* **2015**, *517*, 476.

[26] H. S. Kim, C. R. Lee, J. H. Im, K. B. Lee, T. Moehl, A. Marchioro, S. J. Moon, R. Humphry-Baker, J. H. Yum, J. E. Moser, M. Grätzel, N. G. Park, *Sci. Rep.* **2012**, *2*, 1.

[27] C. H. Chiang, C. G. Wu, *Nat. Photonics* **2016**, *10*, 196.

[28] J. A. Chang, J. H. Rhee, S. H. Im, Y. H. Lee, H. J. Kim, S. Il Seok, M. K. Nazeeruddin, M. Gratzel, *Nano Lett.* **2010**, *10*, 2609.

[29] P. Scherrer, *Kolloidchem. Ein Lehrb.* **1912**, *277*, 387.

[30] A. L. Patterson, *Phys. Rev.* **1939**, *56*, 978.

[31] Q. Zhao, R. Wu, Z. Zhang, J. Xiong, Z. He, B. Fan, Z. Dai, B. Yang, X. Xue, P. Cai, S. Zhan, X. Zhang, J. Zhang, *Org. Electron.* **2019**, *71*, 106.

[32] T. Zhang, N. Guo, G. Li, X. Qian, Y. Zhao, *Nano Energy* **2016**, *26*, 50.

[33] M. van Eerden, M. Jaysankar, A. Hadipour, T. Merckx, J. J. Schermer, T. Aernouts, J. Poortmans, U. W. Paetzold, *Adv. Opt. Mater.* **2017**, *5*, 1.

[34] Y. Wang, T. Gould, J. F. Dobson, H. Zhang, H. Yang, X. Yao, H. Zhao, *Phys. Chem. Chem. Phys.* **2014**, *16*, 1424.

[35] K. Tanaka, T. Takahashi, T. Ban, T. Kondo, K. Uchida, N. Miura,

Solid State Commun. **2003**, *127*, 619.

[36] F. Urbach, *Phys. Rev.* **1953**, *92*, 1324.

[37] T. H. Keil, *Phys. Rev.* **1966**, *144*, 582.

[38] S. De Wolf, J. Holovsky, S. J. Moon, P. Löper, B. Niesen, M. Ledinsky, F. J. Haug, J. H. Yum, C. Ballif, *J. Phys. Chem. Lett.* **2014**, *5*, 1035.

[39] S. A. Moyez, S. Roy, *Sol. Energy Mater. Sol. Cells* **2018**, *185*, 145.

[40] G. J. A. H. Wetzelaer, M. Scheepers, A. M. Sempere, C. Momblona, J. Ávila, H. J. Bolink, *Adv. Mater.* **2015**, *27*, 1837.

[41] D. Luo, R. Su, W. Zhang, Q. Gong, R. Zhu, *Nat. Rev. Mater.* **2020**, *5*, 44.

[42] T. Hwang, B. Lee, J. Kim, S. Lee, B. Gil, A. J. Yun, B. Park, *Adv. Mater.* **2018**, *30*, 1.

[43] W. Xu, Y. Gao, W. Ming, F. He, J. Li, X. H. Zhu, F. Kang, J. Li, G. Wei, *Adv. Mater.* **2020**, *32*, 1.

[44] J. Zhang, H. Yu, *J. Mater. Chem. A* **2021**, *9*, 4138.

[45] V. Sarritzu, N. Sestu, D. Marongiu, X. Chang, S. Masi, A. Rizzo, S. Colella, F. Quochi, M. Saba, A. Mura, G. Bongiovanni, *Sci. Rep.* **2017**, *7*, 1.

[46] K. Tvingstedt, O. Malinkiewicz, A. Baumann, C. Deibel, H. J. Snaith, V. Dyakonov, H. J. Bolink, *Sci. Rep.* **2014**, *4*, 1.

[47] X. Cui, G. Chen, X. Han, *J. Chem. Eng. Data* **2006**, *51*, 1860.

Entry for the Table of Contents

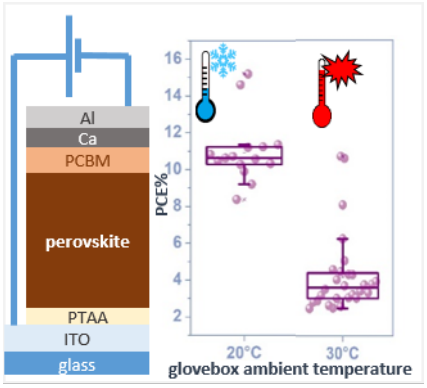

We present that the ambient temperature during the fabrication $CH_3NH_3PbI_3$ (MAPI) thin layer can contribute to the increased density of defects, that can be a source of non-radiative losses in the perovskite solar cells (PSC). As a consequence, the increased trap density within the bandgap of the perovskite leads to a decrease in the overall performance in the PCS.